Semianalytical Model of Multiphase Halbach Array Axial Flux Permanent-Magnet Motor Considering Magnetic Saturation

Du, Yunlu; Huang, Yunkai; Guo, Baocheng; Peng, Fei; Dong, Jianning

DOI
10.1109/TTE.2022.3229051

Publication date
2023

Document Version
Final published version

Published in
IEEE Transactions on Transportation Electrification

Semianalytical Model of Multiphase Halbach Array Axial Flux Permanent-Magnet Motor Considering Magnetic Saturation

Yunlu Du, *Graduate Student Member, IEEE*, Yunkai Huang, Baocheng Guo, *Member, IEEE*, Fei Peng, *Member, IEEE*, and Jianning Dong, *Senior Member, IEEE*

***Abstract*— This article proposes a nonlinear semianalytical model (SAM) of the multiphase Halbach array axial flux permanent-magnet motor (AFPMM) to speed up the computation of its magnetic field. Compared to the existing analytical models, the proposed nonlinear SAM can directly consider magnetic saturation to obtain more accurate results. To this end, the multiphase Halbach array AFPMM is equivalent to several 2-D models by the quasi-3-D method under the Cartesian coordinate system. Then, the nonlinear SAM is developed by using the convolution theorem and the fast Fourier factorization. The proposed nonlinear SAM is studied on a five-phase Halbach array AFPMM with different rotors, and the nonlinear finite element (FE) model and experiment verify its effectiveness. The proposed SAM is computationally efficient and accurate, and it is also applicable to other types of multiphase Halbach array permanent magnet (PM) electrical motors in Cartesian coordinates.**

***Index Terms*— Axial flux permanent-magnet motor (AFPMM), Halbach array, harmonic modeling (HM), nonlinear.**

NOMENCLATURE

AFPMM	Axial flux permanent-magnet motor.
FE	Finite element.
MEC	Magnetic equivalent circuit.
MFD	Magnetic field distribution.
HM	Harmonic modeling.
SAM	Semianalytical model.
rms	Root mean square.

I. INTRODUCTION

AFPMM has the advantages of compact structure, high torque density, high power density, and high efficiency, and has a broad application prospect in electric vehicles and flywheel energy storage systems [1], [2]. Halbach array permanent magnets (PMs') structure has the characteristics of self-shielding magnetization, high sinusoidal magnetic flux density, and low torque ripple, and it is widely used in AFPMM [3], [4], [5]. However, the modeling and optimization of the multiphase Halbach array AFPMM by the 3-D FE model [6], [7] are generally time-consuming due to their complex structure. Therefore, it is of great significance to provide a fast and accurate analytical model for its design and optimization.

Analytical or SAMs, such as the subdomain model and MEC model, are considered to be effective methods for AFPMM design and optimization [8]. In the analytical model, to reduce the calculation time of AFPMM, the 3-D AFPMM model is usually converted into several 2-D models by the quasi-3-D method [9]. Then, the magnetic field and performances of AFPMM can be obtained by the sum of that in each 2-D slice model.

Therefore, the analytical model combining the quasi-3-D method and the Fourier series expansion method has been widely used in the analytical calculation of AFPMM [10], [11], [12]. In [8], based on the coordinate transformation theory, the misalignment problems in the AFPMM are investigated, and the partial magnet demagnetization model is further proposed in [13]. Mohammadi et al. [14] presented a new approach for the analytical modeling of AFPMM by replacing stator teeth with surface currents. As a result, the solution process is simplified compared with the traditional accurate subdomain model. Based on Schwarz–Christoffel mapping, the electromagnetic force of eccentric AFPMM is analyzed in [15]. However, the above analytical model cannot consider the nonlinear effect of iron parts, that is, the saturation is ignored, which leads to the overestimation of the flux density. In addition, as a method to consider the nonlinearity of ferromagnetic materials, the MEC model has been developed to calculate the MFD of AFPMMs [16], [17], [18]. In [16], [17], and [18], the magnetic field of AFPMMs is computed by the quasi-3-D MEC model, and magnetic saturation is considered through nonlinear iterative algorithms. The 3-D MEC model of axial flux machines was further developed by Alipour-Sarabi et al. [19]. Nevertheless, the modeling of the MEC model is usually complex and time-consuming [20], and its accuracy for local saturation calculation is still insufficient.

To solve the aforementioned problems, Sprangers et al. [21] presented the HM technique. The permeability of ferromagnetic materials is expressed with complex Fourier series (CFS) and embedded in the static magnetic field; thus, the saturation

Manuscript received 23 August 2022; revised 20 November 2022; accepted 8 December 2022. Date of publication 14 December 2022; date of current version 13 June 2023. This work was supported in part by the National Natural Science Foundation of China under Grant 52277036. *(Corresponding author: Yunkai Huang.)*

Yunlu Du, Yunkai Huang, and Fei Peng are with the School of Electrical Engineering, Southeast University, Nanjing 210096, China (e-mail: huangyk@seu.edu.cn).

Baocheng Guo is with the School of Electrical and Automation Engineering, Nanjing Normal University, Nanjing 210023, China (e-mail: guobaocheng1986@gmail.com).

Jianning Dong is with the Department of Electrical Sustainable Energy, Delft University of Technology, 2628 DC Delft, The Netherlands (e-mail: j.dong-4@tudelft.nl).

Digital Object Identifier 10.1109/TTE.2022.3229051

effect can be considered by iterative calculation. This scientific research has been applied to many kinds of PM motors by Djelloul-Khedda et al. [22], [23], and [24]. Zhao et al. [25] and [26] further divided the iron parts along with normal and tangential directions and carried out a multiobjective optimization design for a Vernier machine and coaxial magnetic gears, and its computation time is only about 80% of the FE model. Zhao et al. [20] and Guo et al. [27] further extended the HM technique to Cartesian coordinates for AFPMM calculation.

On the other hand, the analytical modeling of the Halbach array PM motor is mainly studied in the radial flux motor [28], [29], [30], while the axial flux motor is rarely studied. Therefore, for structurally complex multiphase Halbach array AFPMM, the HM technique applied for its modeling and considering local saturation remains to be explored.

In this article, a nonlinear SAM of the five-phase Halbach array AFPMM is developed to speed up the calculation of its magnetic field, and its computation time is about one-fourth of that of the 3-D FE model. To consider the magnetic saturation, the iron parts are divided into smaller parts along with normal and tangential directions, and then, the nonlinear effect of the stator teeth can be solved by an iterative algorithm. Then, the electromagnetic performance of the studied five-phase Halbach array AFPMM with different magnetization directions is calculated and compared with the FE model. Finally, a prototype with the magnetization direction of 35° or 45° is manufactured, and the correctness of the nonlinear SAM developed is further verified by the experimental results. Moreover, the nonlinear SAM proposed in this article has certain universality for AFPMM with Halbach array structure with different magnetic pole combinations, magnetization angles, and magnetization directions, and has significant theoretical value and engineering reference significance for its design and optimization.

This article is organized as follows. Section II introduces the nonlinear SAM of the five-phase Halbach array AFPMM. In Section III, an iterative algorithm considering the nonlinearity of ferromagnetic materials is proposed. Section IV compares the results of the SAM and the FE results with different magnetization directions (i.e., 35°, 45°, and 60°). Then, in Section V, the experimental results of a prototype with the magnetization direction of 35° or 45° are compared.

II. Model of Halbach Array AFPMM

In this section, to reduce computation time, a 3-D AFPMM model is converted to several 2-D calculation slices by the quasi-3-D method. Then, according to the HM technology, the SAM of the multiphase Halbach array AFPMM is proposed.

A. Model Simplification

This article introduces a five-phase 10/4 Halbach array AFPMM with concentrated winding to illustrate the universality of the developed SAM. Table I lists the main geometric parameters of the studied motor.

Simplifying the 3-D magnetic field problem to a 2-D problem is the key to accelerating the MFD calculation of the AFPMM. Thus, as shown in Fig. 1, the 3-D AFPMM model is converted to several 2-D slice models [8]. The studied AFPMM is divided into n_s slices, and the average radius R^s_{av} and width t_{cp} of the sth slice are given by

$$R^s_{\text{av}} = R_i + \frac{R_o - R_i}{n_s}\left(s - \frac{1}{2}\right) \tag{1}$$

$$t_{\text{cp}} = \frac{R_o - R_i}{n_s}. \tag{2}$$

Similar to the traditional analytical model, the nonlinear SAM proposed in this article is also based on certain assumptions, such as ignoring the end effect. These assumptions can be found in [20] and will not be repeated here. In this way, the analytical model of the 2-D slice model is established in the 2-D Cartesian coordinate system.

Then, the 2-D analytical model of each slice can be divided into the following simple regions: the rotor backplate region, the PMs region, the air-gap region, the stator slots/teeth region, and the stator yoke region, as shown in Fig. 2.

B. Semianalytical Model

The solutions of the Laplace equation or Poisson equation of each calculation region are shown in the following.

TABLE I
PARAMETERS OF FIVE-PHASE HALBACH ARRAY AFPMM

AFPMM Quantity	Symbol	Value
Number of pole pairs	p	2
Number of slots	Q	10
Rated power	P	10 kW
Rated current	I	20 A
Length of air-gap	g	3 mm
Magnet height	h_m	6 mm
Remanence of magnet	B_r	0.76/1.25 T
Magnet type	-	Bonded/Sintered
Outer/Inner radius of AFPMM	R_o/R_i	100/50 mm
Number of turns per slot	N_c	116

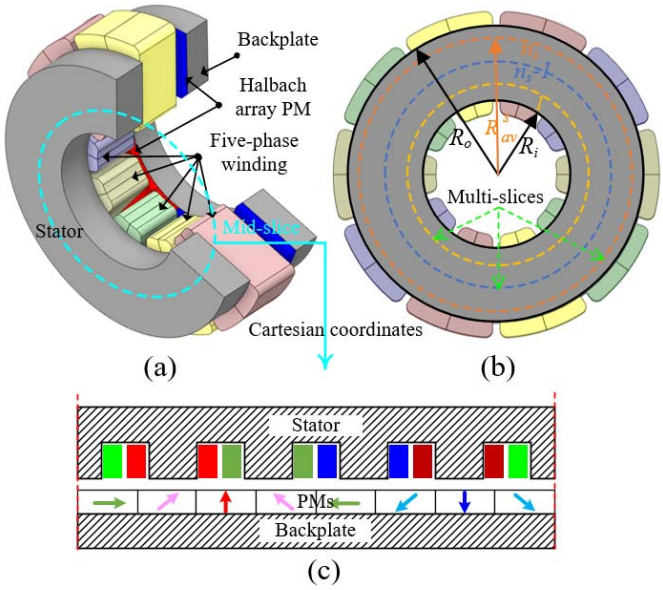

Fig. 1. Prototype of five-phase Halbach array AFPMM. (a) Studied machine. (b) Multislices model. (c) Expansion of mid-slice.

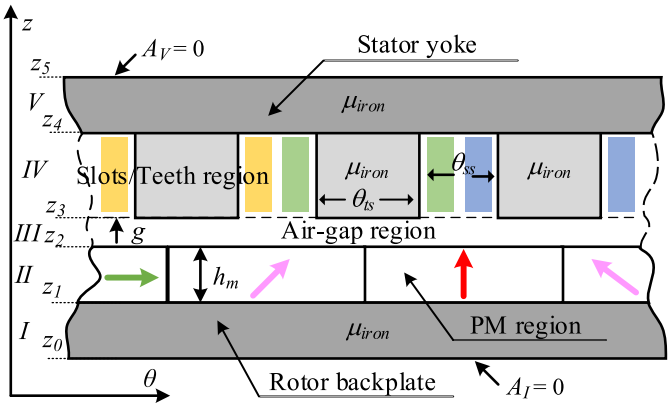

Fig. 2. 2-D analytical model.

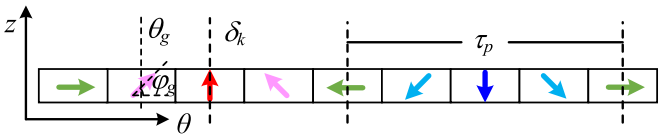

Fig. 3. Halbach array PMs.

1) Air-Gap Region: In the air-gap region, the magnetic vector potential A_{III} satisfies the following Laplace's matrix equation:

$$\frac{\partial^2 A_{\mathrm{III}}}{\partial z^2} - \frac{1}{R_m^2} V_{\mathrm{III}}^2 A_{\mathrm{III}} = 0. \tag{3}$$

The general solution to (3) can be written as

$$A_z^{\mathrm{III}} = e^{\frac{V_{\mathrm{III}}}{R_m} z} C_1 + e^{-\frac{V_{\mathrm{III}}}{R_m} z} C_2. \tag{4}$$

The following notation is used to simplify the expression of general solutions for different regions [27]:

$$E(\omega, \alpha, \beta, \gamma) = \left(\frac{e^{\beta/\alpha}}{e^{\gamma/\alpha}}\right)^{\omega}. \tag{5}$$

Then, the general solution of region III can be obtained

$$A_z^{\mathrm{III}} = R_m \cdot E(V_{\mathrm{III}}, R_m, z, z_3) a_2 + R_m \cdot E(V_{\mathrm{III}}, R_m, z_2, z) b_2 \tag{6}$$

where $V_{\mathrm{III}} = |K_\theta|$ and a_3 and b_3 are unknown coefficients.

2) Stator Yoke and Rotor Backplate Regions: Similar to the air-gap region, the stator yoke and the rotor backplate satisfy the Laplace equation, and their general solutions are

$$A_z^{\mathrm{V}} = R_m \cdot E(K_\theta, R_m, z, z_5) a_5 + R_m \cdot E(K_\theta, R_m, z_4, z) b_5 \tag{7}$$

$$A_z^{\mathrm{I}} = R_m \cdot E(K_\theta, R_m, z, z_1) a_1 + R_m \cdot E(K_\theta, R_m, z_0, z) b_1 \tag{8}$$

where a_1, b_1, a_5, and b_5 are unknown coefficients.

3) PM Region: The Halbach array AFPMM studied in this article has four blocks per pole, and the magnetization direction of each PM is φ_g [29], as shown in Fig. 3.

The center position of the mth normal magnetized PM is

$$\begin{cases} \delta_k = \dfrac{2\pi}{p}(m-1) + \delta_0 \\ m = 1, 2, \ldots, p \end{cases} \tag{9}$$

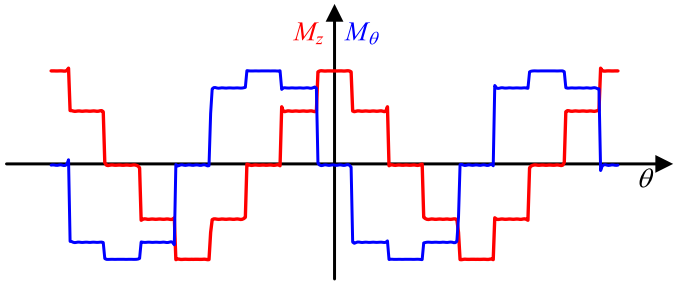

Fig. 4. Components of M.

where δ_0 is the initial angular position of the rotor and p is the number of pole pairs.

The center position θ_g of the gth PM is defined as

$$\begin{cases} \theta_g = \dfrac{\pi(g-1)}{pG} \\ g = 1, 2, \ldots, 2G \end{cases} \tag{10}$$

where G represents the number of blocks.

Then, the Fourier coefficients $\hat{M}_{z,n}$ and $\hat{M}_{\theta,n}$ can be obtained by

$$\hat{M}_{z,n} = \frac{1}{2\pi jn} \sum_{m=1}^{p} \sum_{g=1}^{2G} \frac{B_{\mathrm{rem}}}{\mu_0} \cos(\varphi_g) \times \left\{ e^{jn\frac{(2g-1)\pi}{2pG}} - e^{jn\frac{(2g-3)\pi}{2pG}} \right\} e^{jn\delta_k}, \quad n \neq 0 \tag{11}$$

$$\hat{M}_{\theta,n} = \frac{1}{2\pi jn} \sum_{m=1}^{p} \sum_{g=1}^{2G} \frac{B_{\mathrm{rem}}}{\mu_0} \sin(\varphi_g) \times \left\{ e^{jn\frac{(2g-1)\pi}{2pG}} - e^{jn\frac{(2g-3)\pi}{2pG}} \right\} e^{jn\delta_k}, \quad n \neq 0. \tag{12}$$

When the magnetization direction is 35°, the components of the magnetization vector M are given in Fig. 4.

In the PM region, the magnetic vector potential A_{II} satisfies the following Poisson's matrix equation:

$$\frac{\partial^2 A_{\mathrm{II}}}{\partial z^2} - \frac{1}{R_m^2} V_{\mathrm{II}}^2 A_{\mathrm{II}} = -j \frac{\mu_0}{R_m} \mu_{c,\theta}^{\mathrm{II}} K \left(\mu_{c,z}^{\mathrm{II}}\right)^{-1} M_z. \tag{13}$$

The general solution to (13) can be obtained as

$$A_{z,\mathrm{com}}^{\mathrm{II}} = R_m \cdot E(V_{\mathrm{II}}, R_m, z, z_2) a_2 + R_m \cdot E(V_{\mathrm{II}}, R_m, z_1, z) b_2 \tag{14}$$

where a_2 and b_2 are unknown coefficients.

The particular solution of the PM region is

$$A_{z,\mathrm{par}}^{\mathrm{II}} = j\mu_0 \left(V_{\mathrm{II}}^2\right)^{-1} \mu_{c,\theta}^{\mathrm{II}} K \left(\mu_{c,z}^{\mathrm{II}}\right)^{-1} M_z. \tag{15}$$

Then, the solution of the PM region is obtained by

$$A_z^{\mathrm{II}} = A_{z,\mathrm{com}}^{\mathrm{II}} + A_{z,\mathrm{par}}^{\mathrm{II}}. \tag{16}$$

4) Slots/Teeth Region: The multiphase motor studied in this article is a five-phase AFPMM with concentrated winding, as shown in Fig. 5.

The angular position of each slot winding is defined by [22]

$$\begin{cases} \alpha_i = \dfrac{2\pi}{Q} i - \dfrac{\pi}{Q} \\ i = 1, 2, \ldots, Q \end{cases} \tag{17}$$

where Q is the number of slots.

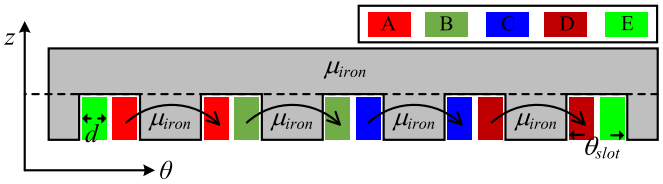

Fig. 5. Distribution of five-phase winding.

The Fourier coefficients of $\hat{J}_{y,n}$ can be obtained by

$$\hat{J}_{y,n} = \frac{1}{2\pi jn}\sum_{i=1}^{Q_s}\Big[J_{i,1}\big(e^{jnd}-1\big)e^{-jn\frac{\theta_{ss}}{2}} + J_{i,2}\big(1-e^{-jnd}\big)e^{jn\frac{\theta_{ss}}{2}}\Big]e^{jn\alpha_i} \quad (18)$$

$$J_{i,1} = \frac{N_c}{S}C_1^T[i_A, i_B, i_C, i_D, i_E] \quad (19)$$

$$J_{i,2} = \frac{N_c}{S}C_2^T[i_A, i_B, i_C, i_D, i_E]. \quad (20)$$

In the slots/teeth region, the magnetic vector potential A_{IV} satisfies the following Poisson's matrix equation:

$$\frac{\partial^2 A_{\mathrm{IV}}}{\partial z^2} - \frac{1}{R_m^2}V_{\mathrm{IV}}^2 A_{\mathrm{IV}} = -\mu_{c,\theta}^{\mathrm{IV}} J. \quad (21)$$

The general solution of the slots/teeth region can be obtained as

$$A_{z,\mathrm{com}}^{\mathrm{IV}} = R_m \cdot E(V_{\mathrm{IV}}, R_m, z, z_4)a_4 + R_m \cdot E(V_{\mathrm{IV}}, R_m, z_3, z)b_4 \quad (22)$$

where a_4 and b_4 are unknown coefficients.

The particular solution of slots/teeth region is

$$A_{z,\mathrm{par}}^{\mathrm{IV}} = R_m^2 V_{\mathrm{IV}}^{-2}\mu_{c,\theta}^{\mathrm{IV}} J. \quad (23)$$

Then, the solution of slots/teeth region is obtained by

$$A_z^{\mathrm{IV}} = A_{z,\mathrm{com}}^{\mathrm{IV}} + A_{z,\mathrm{par}}^{\mathrm{IV}}. \quad (24)$$

5) Boundary Conditions: Based on the general solutions of the above five subdomains, the continuous boundary conditions are listed as follows:

$$\begin{cases} A_z^{\mathrm{I}}\big|_{z=z_1} - A_z^{\mathrm{II}}\big|_{z=z_1} = 0, & H_\theta^{\mathrm{I}}\big|_{z=z_1} - H_\theta^{\mathrm{II}}\big|_{z=z_1} = 0 \\ A_z^{\mathrm{II}}\big|_{z=z_2} - A_z^{\mathrm{III}}\big|_{z=z_2} = 0, & H_\theta^{\mathrm{II}}\big|_{z=z_1} - H_\theta^{\mathrm{III}}\big|_{z=z_1} = 0 \\ A_z^{\mathrm{III}}\big|_{z=z_3} - A_z^{\mathrm{IV}}\big|_{z=z_3} = 0, & H_\theta^{\mathrm{III}}\big|_{z=z_3} - H_\theta^{\mathrm{IV}}\big|_{z=z_3} = 0 \\ A_z^{\mathrm{IV}}\big|_{z=z_4} - A_z^{\mathrm{V}}\big|_{z=z_4} = 0, & H_\theta^{\mathrm{IV}}\big|_{z=z_4} - H_\theta^{\mathrm{V}}\big|_{z=z_4} = 0. \end{cases} \quad (25)$$

Furthermore, the Dirichlet boundary conditions are set at $z = z_0$ and $z = z_5$ [31]

$$\begin{cases} A^{\mathrm{I}}\big|_{z=z_0} = 0 \\ A^{\mathrm{V}}\big|_{z=z_5} = 0. \end{cases} \quad (26)$$

Finally, all boundary conditions are written in the following matrix form:

$$MX = Y \quad (27)$$

where M, X, and Y are the coefficient factors, the unknown coefficients, and the constant values in the boundary condition equations, respectively.

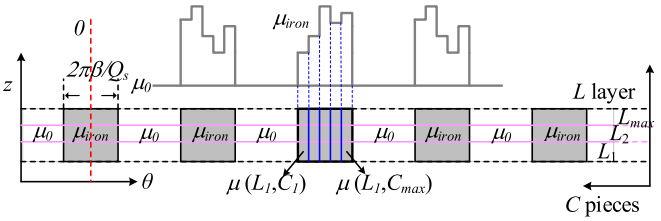

Fig. 6. Multilayer division of stator teeth.

III. Proposed Nonlinear Algorithm Considering Magnetic Saturation

In this section, the nonlinear solution algorithm is used to estimate the saturation level of the stator tooth, and this is due to the stator tooth having an obvious magnetic saturation phenomenon.

For the slots/teeth region, each stator tooth is divided into C_T blocks along the θ-direction and L layers along the z-direction, and the permeability distribution is shown in Fig. 6. The permeability can be expressed by CFS

$$\mu^l(\theta) = \sum_{n=-N}^{n=N}\hat{\mu}_n^l e^{-jn\theta}. \quad (28)$$

Then, the Fourier coefficients of the lth layer of region III can be obtained

$$\hat{\mu}_n^l = \begin{cases} (1-\beta)\mu_0 + \dfrac{\beta}{Q_s C_T}\displaystyle\sum_{i=1}^{Q}\sum_{c=1}^{C_T}\mu_{i,c}, & n=0 \\ \displaystyle\sum_{i=1}^{Q}\frac{\mu_0}{2\pi jn}e^{jn\pi\frac{2(i-1)-\beta}{Q}}\Big[1-e^{jn\pi\frac{2(\beta-1)}{Q}}\Big] \\ \quad +\displaystyle\sum_{i=1}^{Q}\sum_{c=1}^{C_T}\frac{\mu_{i,c}}{2\pi jn}e^{\frac{\beta C_T-2(i-1)C_T-2\beta c}{QC_T}}\Big[e^{jn\pi\frac{2\beta}{QC_T}}-1\Big], & n\neq 0 \end{cases} \quad (29)$$

where $\mu_{i,c}$ is the permeability in the cth piece of the ith tooth.

The Fourier coefficients $\hat{\mu}_n^{l,\mathrm{rec}}$ can be obtained by replacing $(\mu_0, \mu_{i,c})$ by $(1/\mu_0, 1/\mu_{i,c})$ in (29).

Normal and tangential permeability convolution matrices can be obtained by using Cauchy's product theorem

$$\mu_{c,z} = \begin{bmatrix} \hat{\mu}_0 & \cdots & \hat{\mu}_{-2N} \\ \vdots & \ddots & \vdots \\ \hat{\mu}_{2N} & \cdots & \hat{\mu}_0 \end{bmatrix}, \quad \mu_{c,\theta} = \begin{bmatrix} \hat{\mu}_0^{\mathrm{rec}} & \cdots & \hat{\mu}_{-2N}^{\mathrm{rec}} \\ \vdots & \ddots & \vdots \\ \hat{\mu}_{2N}^{\mathrm{rec}} & \cdots & \hat{\mu}_0^{\mathrm{rec}} \end{bmatrix}^{-1}. \quad (30)$$

As shown in Fig. 6, the permeability of each tooth is discretized along the z- and θ-directions. On the other hand, although the calculation accuracy can be improved by dividing the iron parts into more layers, it sacrifices the calculation time [26].

Fig. 7 shows the iteration process. k in Fig. 7 is the correction factor ($0 < k < 1$), and the empirical value is generally 0.2–0.3. First, according to the μ_r–B curve, the relative permeability of ferromagnetic materials is set to the maximum (i.e., $\mu_{r,\max} = 4500$). Then, the magnetic flux density $B_{i,c}$ of each tooth can be obtained by solving (27), and then, the permeability is iteratively updated. When the

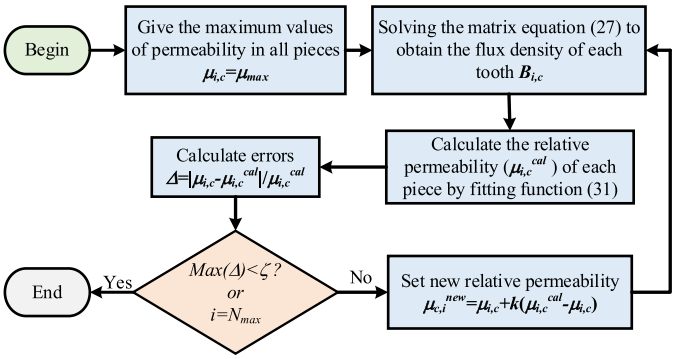

Fig. 7. Nonlinear iterative algorithm.

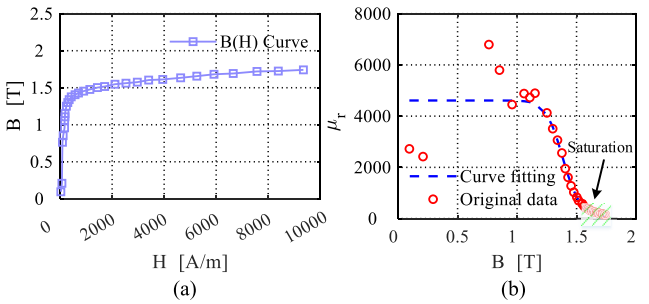

Fig. 8. Nonlinear characteristic of 2605SA1 amorphous alloys. (a) B–H. (b) μ_r–B.

calculation error of relative permeability Δ meets the error requirement or reaches the maximum iteration number, the nonlinear iteration ends.

The relative permeability can be obtained by the fitting equation [32]

$$\mu_r(B) = \left(\frac{B_o}{H_o\mu_0}\right)\left(\frac{1}{1+(B/B_o)^{\upsilon-1}}\right) \tag{31}$$

where B_o, H_o, and υ are the constants.

The stator material of AFPMM in this article is 2605SA1 amorphous alloy, and the fitting curve is shown in Fig. 8. The parameters B_o, H_o, and υ are 1.388, 239.571, and 19.985, respectively. Although the fitting curve has errors when the flux density is lower than 1.2 T, the material is not saturated at this time. It should be pointed out that this article mainly studies the effect of ferromagnetic materials in the magnetic saturation state on the MFD. With the increase in magnetic density, the fitting curve is consistent with the original data.

IV. FE Model Verification

To illustrate the computational capability of SAM, the results of flux density and performances (i.e., back EMF, cogging torque, and electromagnetic torque) calculated by SAM under different magnetization directions (i.e., 35°, 45°, and 60°) are compared with the results calculated by the FE model.

A. FE Model

Fig. 9 shows the 3-D FE model of the five-phase Halbach array AFPMM studied in this article, and the stator teeth exhibit a noticeable saturation behavior when the phase current peak is 30 A.

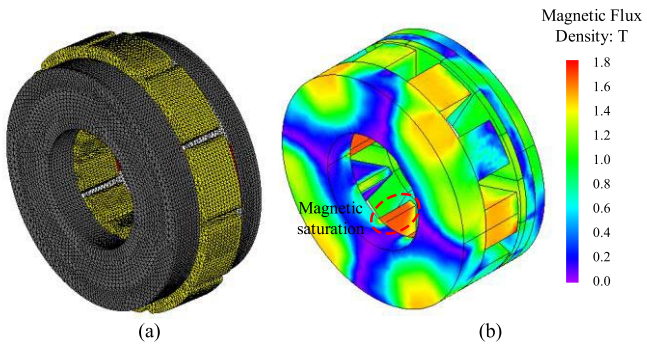

Fig. 9. 3-D FE model. (a) Mesh. (b) Magnetic flux density distribution.

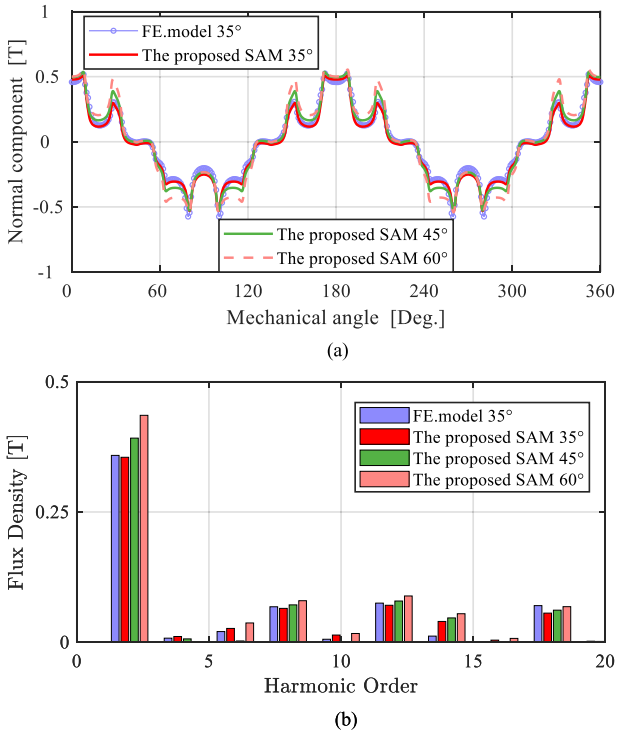

Fig. 10. Comparison of the normal component of the no-load flux density at $z = (z_2 + z_3)/2$. (a) Waveforms. (b) Harmonic spectrum.

To illustrate the computation accuracy of the SAM, the rms error is adopted as the evaluation standard, and 360 calculation points (i.e., $N_{pc} = 360$) along the circumferential direction are taken to calculate the rms error

$$\text{RMS error} = \sqrt{\frac{\sum_{i=1}^{N_{pc}}\left(B_i^{FEA} - B_i^{HM}\right)^2}{N_{pc}}}. \tag{32}$$

B. Comparison of MFD

Figs. 10 and 11 show the waveforms and harmonic spectrums of the normal and tangential components of the air-gap flux density in different magnetization directions. To avoid repetition, only the magnetization direction of 35° is given in the FE model. It can be seen from the comparison that the waveforms obtained by the two calculation methods are very consistent, and the harmonic times are also very close. The rms error of the normal component (i.e., Fig. 10) and tangential component (i.e., Fig. 11) is 17.3 and 11.6 mT, respectively.

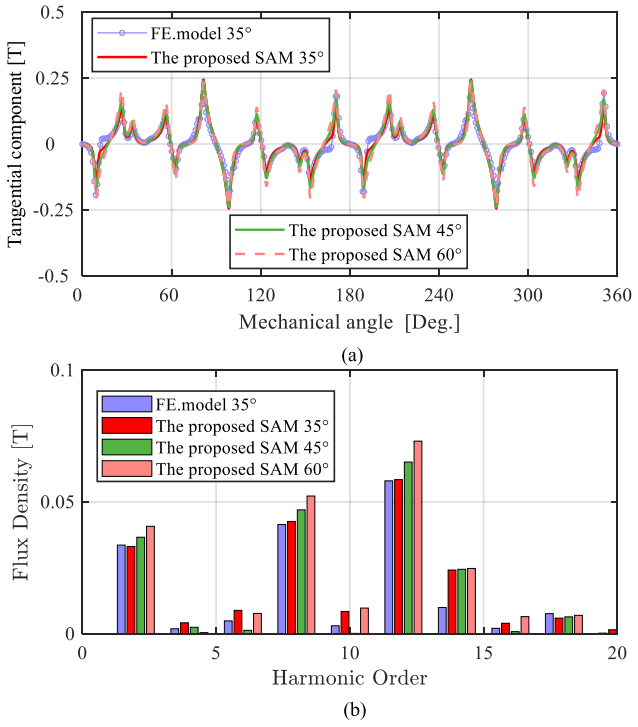

Fig. 11. Comparison of the tangential component of the no-load flux density at $z = (z_2 + z_3)/2$. (a) Waveforms. (b) Harmonic spectrum.

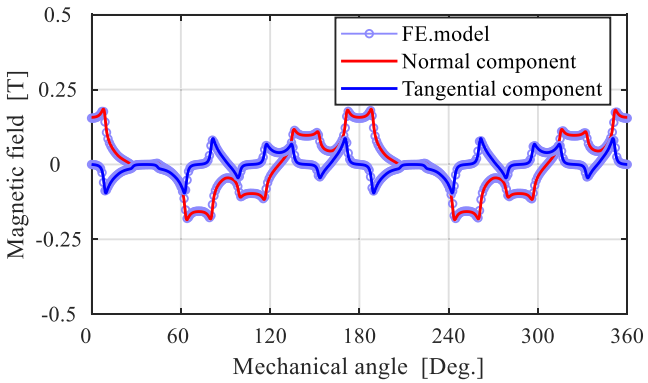

Fig. 12. Comparison of flux density components at $z = (z_2 + z_3)/2$ (armature reaction).

To verify the armature reaction field, the currents of five-phase coils are set as $i_a = 0$, $i_b = -19.02$, $i_c = -11.76$, $i_d = 11.76$, and $i_e = 19.02$ A. In addition, this ignores the influence of the magnetization source (i.e., $B_r = 0$ T). In Fig. 12, the comparison of flux density components at $z = (z_2 + z_3)/2$ under the armature magnetic field is given. The flux density estimated by the SAM is essentially compatible with the FE model, with rms errors of 5.8 and 5.2 mT.

In the above comparison, the stator tooth does not appear magnetic saturation. Therefore, both the proposed SAM and the traditional analytical model ($\mu_r \to \infty$) have high calculation accuracy. However, as shown in Fig. 9, the teeth will have an obvious magnetic saturation phenomenon under load operation ($I_{\text{peak}} = 30$ A). At this time, the traditional subdomain model will increase the calculation error of the magnetic field. In Figs. 13 and 14, the magnetic flux density waveforms and harmonic spectrums under load conditions are compared. The rms errors of Figs. 13 and 14 are 28.4 and

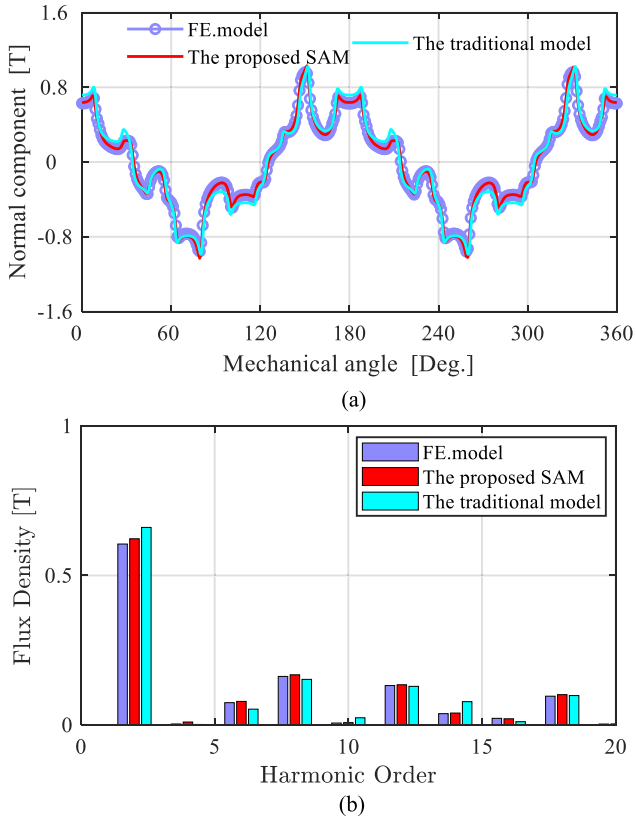

Fig. 13. Comparison of normal components of the load flux density at $z = (z_2 + z_3)/2$ (magnetization direction 35°). (a) Waveforms. (b) Harmonic spectrum.

20.6 mT calculated by nonlinear SAM, and 59.2 and 36.4 mT calculated by the traditional model. The rms errors of the flux density components show that the traditional subdomain model has large calculation errors because the traditional subdomain model assumes that the ferromagnetic material has infinite relative permeability. In this article, the influence of magnetic saturation is considered through the nonlinear iterative algorithm proposed in Section III, so the computation accuracy is improved.

C. Comparison of Electromagnetic Performances in Different Magnetization Directions

The output torque of the studied five-phase Halbach array AFPMM can be obtained by the following equation [13]:

$$T = \frac{LR_m^2}{\mu_0} \int_0^{2\pi} B_n(R_m, \theta) \cdot B_t(R_m, \theta) d\theta \tag{33}$$

where L and R_m are the radial length and radius of the computed slice, respectively.

The cogging torques of the studied five-phase Halbach array AFPMM with different magnetization directions (i.e., 35°, 45°, and 60°) are shown in Fig. 15. Thus, the proposed SAM can predict cogging torque with high precision when the PMs have different magnetization directions.

Fig. 16 shows the electromagnetic torque waveforms with different magnetization directions (i.e., 35°, 45°, and 60°). Although there exists little amplitude difference in the on-load torque waveforms between the proposed SAM and FE models,

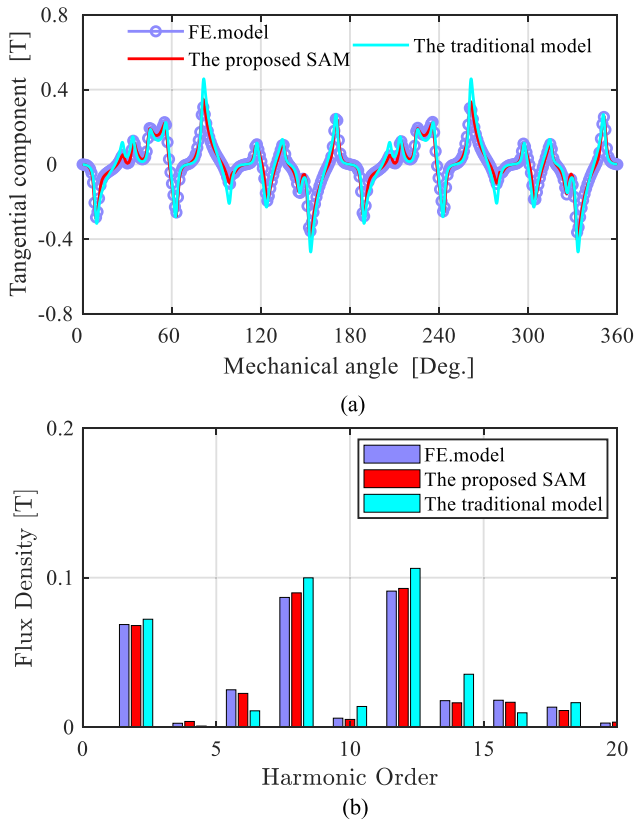

Fig. 14. Comparison of tangential components of the load flux density at $z = (z_2 + z_3)/2$ (magnetization direction 35°). (a) Waveforms. (b) Harmonic spectrum.

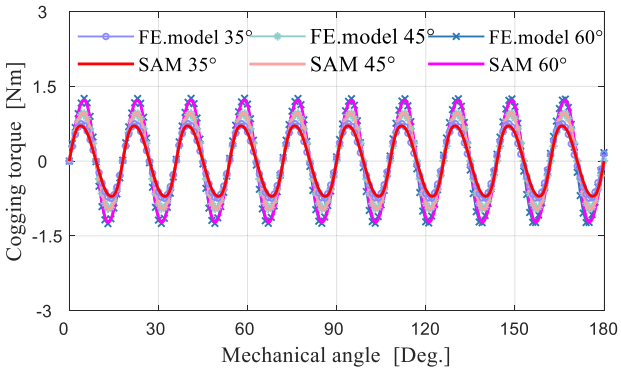

Fig. 15. Cogging torque in different magnetization directions.

the variation trends for them are the same. The relative error is 4.65% under rated conditions ($I_{\text{peak}} = 20$ A).

The flux linkage of phase A can be obtained by [27]

$$\varphi_a = L\frac{N_c}{S}\sum_{i=1}^{Q_s}\int_{\alpha_i+\frac{\theta_{ss}}{2}-d}^{\alpha_i+\frac{\theta_{ss}}{2}}\int_{z_2}^{z_3} A_z^{\text{III}}(z,\theta)dzd\theta. \tag{34}$$

Then, according to the magnetic theory, the back EMF can be computed as

$$E_a = -\frac{d\varphi_a}{dt}. \tag{35}$$

Fig. 17 shows the comparison of back EMFs with different magnetization directions. The back EMF waveforms predicted by the nonlinear SAM are consistent with the results of the FE

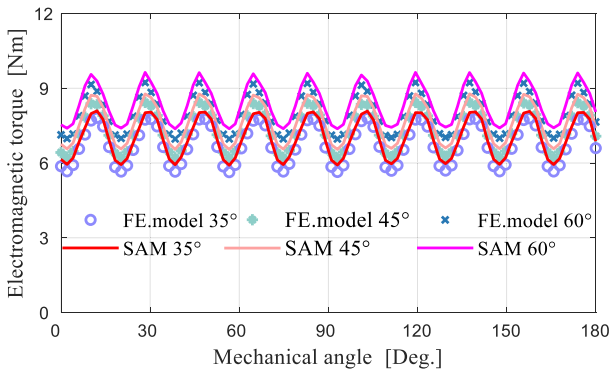

Fig. 16. Comparison of electromagnetic torque in different magnetization directions ($I_{\text{peak}} = 20$ A).

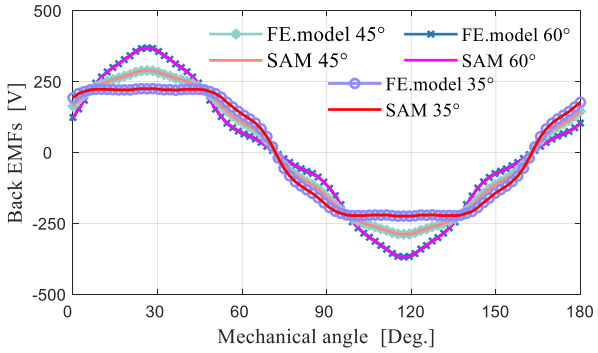

Fig. 17. Comparison of back EMFs (15 000 r/min) with different magnetization directions.

model. In addition, the distortion and harmonics of the back EMF change with the magnetization direction.

D. Iron Loss Computation

The traditional analytical model assumes that the relative permeability of ferromagnetic material is infinite, which leads to natural defects in the calculation of core loss. However, the nonlinear SAM proposed in this article can accurately calculate the MFD of iron parts, which has potential applications in the calculation of core loss. The losses of the iron core can be calculated by the Steinmetz model [24], which are expressed as

$$P_{\text{iron}} = k_h f \hat{B}^{a+b\cdot\hat{B}} + k_e f^2 \hat{B}^2 \tag{36}$$

where k_h, k_e, a, and b are unknown coefficients determined by the type of ferromagnetic material. For the 2605SA1 amorphous alloy material used in this article, the values are 1.107e^{-2}, 8.738e^{-6}, 2.833, and 0.714.

Taking the stator tooth as an example to calculate the iron loss, the iron loss of the stator yoke and the rotor backplate can be calculated by the same method. For each stator tooth, four sampling points are selected, and Fig. 18 shows the waveforms and loci of the magnetic flux density at points $P^1_{i,\text{tooth}}$ and $P^3_{i,\text{tooth}}$ for an entire electrical period. It can be seen that the magnetic flux density and loci of point $P^3_{i,\text{tooth}}$ are very consistent with the FE model, but point $P^1_{i,\text{tooth}}$ has errors. These errors will affect the estimation of iron loss. Fig. 19 shows the calculation results of iron loss under different currents. When the peak current is 8 A, the maximum relative error is 8.69%. The calculation error can be further reduced by selecting more sampling points on the stator teeth.

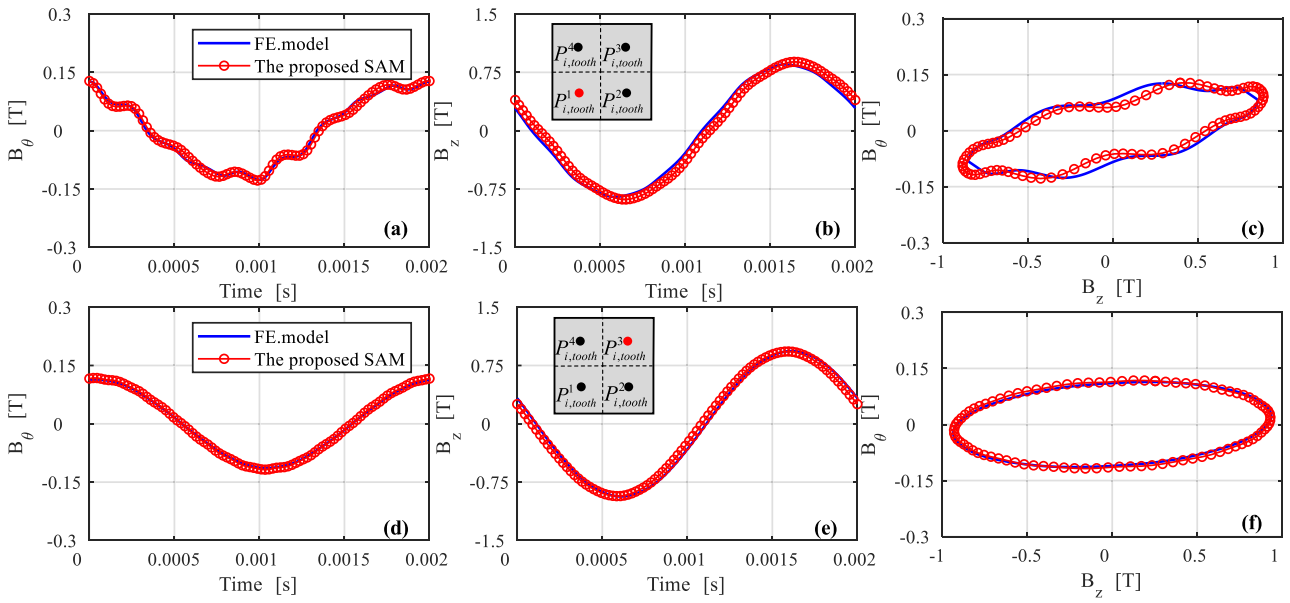

Fig. 18. On-load ($I_{\text{peak}} = 8$ A) evolution of magnetic flux density for two points on the stator tooth. (a) and (d), (b) and (e), and (c) and (f) Tangential component, normal component, and loci of magnetic flux density of point $P^1_{i,\text{tooth}}$ and point $P^3_{i,\text{tooth}}$, respectively.

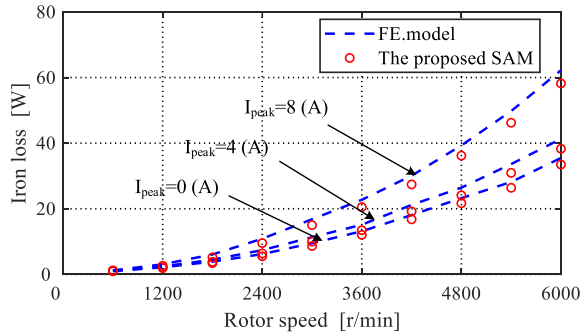

Fig. 19. Comparison of iron losses predicted by the proposed SAM and FE model.

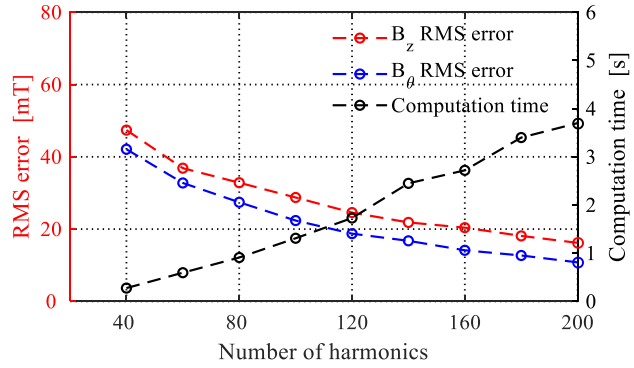

Fig. 20. Influence of the harmonics number on the computation time and accuracy ($I_{\text{peak}} = 0$ A).

E. Computation Time

To illustrate the computation time, the computation time of one calculation slice is selected as a comparison in the proposed SAM, and the maximum spatial harmonic order is set to $N = 200$. On the other hand, to speed up the calculation of the 3-D FE model, the mesh is sparse, with only 104 897 mesh elements. Table II shows the computation time between the nonlinear SAM, linear SAM, and 3-D FE model for an electric period with 120 steps. Thus, compared

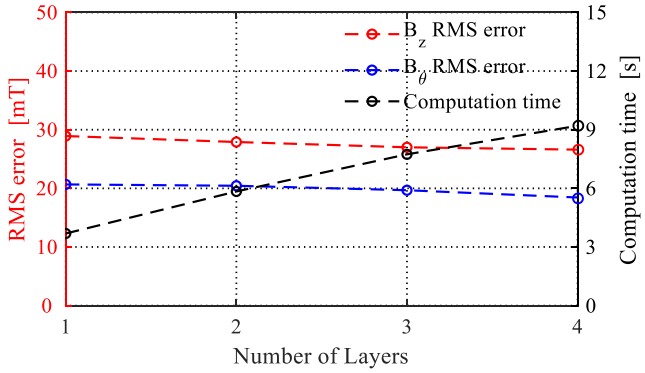

Fig. 21. Influence of different layer numbers of stator teeth on computation time and accuracy ($I_{\text{peak}} = 30$ A).

with the nonlinear 3-D FE model, the proposed nonlinear SAM only takes about one-fourth of the time, while the linear SAM (without considering magnetic saturation) has a shorter calculation time. Figs. 20 and 21 show the effects of different harmonic orders and stator tooth layers on the calculation time and accuracy of each step. Although the rms error is reduced by 15% for harmonics $N = 120$–200, the calculation time is increased from 1.73 to 3.70 s/step. At $N = 200$, when the number of stator tooth layers increases from 1 to 4, the rms errors of the normal and tangential components are reduced by 8.7% and 12.1%, respectively, but the calculation time is increased from 3.7 to 9.2 s/step. This is due to the fact that $2 \times (2 \times N + 1)$ extra unknown coefficients are introduced for each additional calculation region. Although increasing the number of harmonics or the calculation regions will increase computation accuracy to some extent, the Gibbs phenomenon caused by the decomposition of CFS will lead to a decrease in calculation speed and slow convergence, which will inevitably lead to computation error [31].

To obtain higher calculation accuracy, the SAM proposed in this article needs to select the appropriate calculation section

TABLE II
COMPARISON OF COMPUTATION TIME

	Harmonic	Elements	Computation time
3D FE model	-	104897	1h22min
Nonlinear SAM	200	-	24min18s
Linear SAM	200	-	6min24s

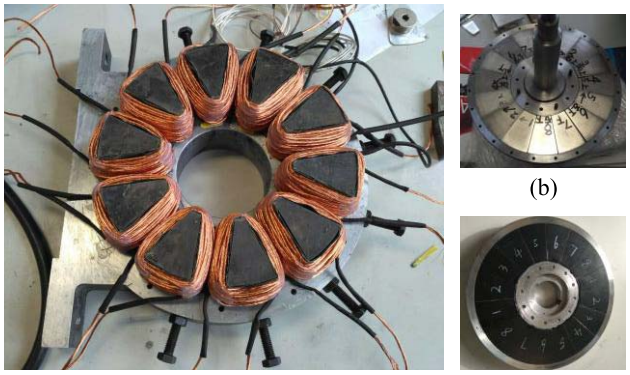

Fig. 22. Stator and rotor of Halbach array AFPM machine. (a) Stator. (b) Rotor (sintered, magnetization direction 45°). (c) Rotor (bonded, magnetization direction 35°).

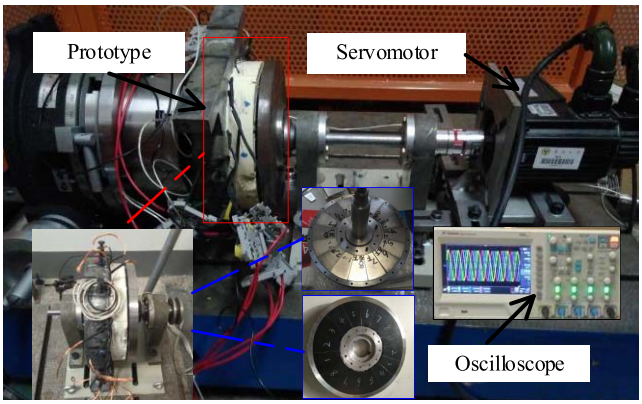

Fig. 23. Back EMFs experimental setup.

according to the specific axial flux motor structure. For the 3-D FE model, it is necessary to encrypt the mesh to obtain more accurate calculation results. The above operations will undoubtedly increase the calculation time, but compared with the 3-D FE model, the SAM will also greatly shorten the calculation time. The linear SAM will play an important role in the initial design stage of the multiphase Halbach array AFPMM, and the calculation of the magnetic field can be further accelerated by reducing the number of calculated slices or spatial harmonics. Therefore, the proposed SAM for the magnetic field calculation of the multiphase Halbach array AFPMM has great engineering application value for its design and optimization (e.g., combined with the NSGA-II algorithm), which will greatly reduce the calculation time.

V. EXPERIMENTAL VERIFICATION

In this section, a five-phase Halbach array AFPMM with a magnetization direction of 35° or 45° is investigated. The stator and rotor are shown in Fig. 22.

The back EMF experimental platform of the studied five-phase Halbach array AFPMM is shown in Fig. 23.

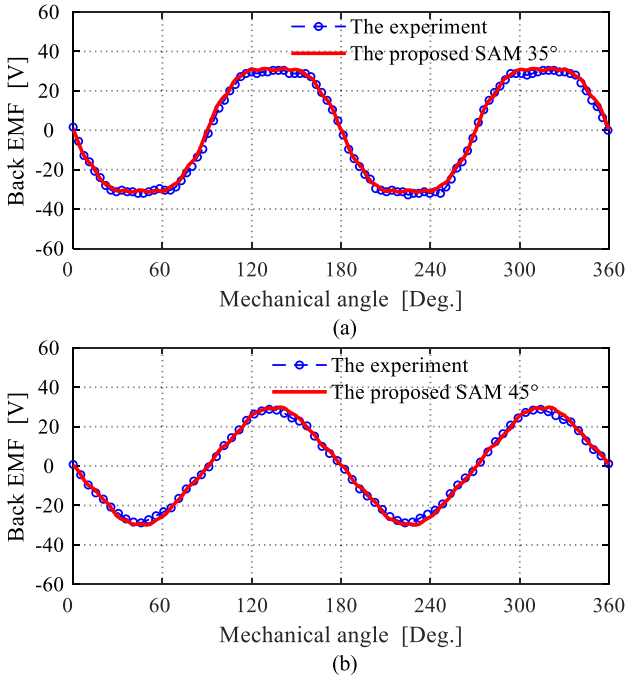

Fig. 24. Back EMF results. (a) 2000 r/min (bonded, magnetization direction 35°). (b) 1500 r/min (sintered, magnetization direction 45°).

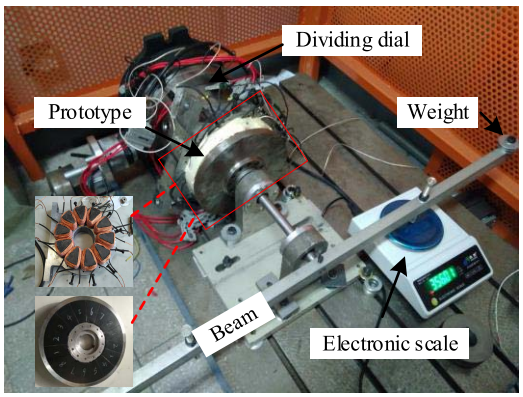

Fig. 25. Cogging torque experimental setup (bonded, magnetization direction 35°).

The prototype is connected with the servomotor through a coupling, and the oscilloscope (InfiniiVision DSOX2024A, the bandwidth is 200 MHz and the maximum sample rate is 2 GSa/s) is used to measure the back EMFs. For two types of rotors, the back EMF was tested at 1500 r/min (Sintered, magnetization direction 45°) and 2000 r/min (Bonded, magnetization direction 35°), respectively, as shown in Fig. 24(a) and (b). It can be seen that the back EMF waveforms predicted by the SAM are consistent with the experimental results. Taking bonded NdFeB (magnetization direction 45°) as an example, the rms value of the experimental result is 19.67 V, while the value computed by the proposed SAM is 20.38 V, and the relative error is only 3.6%. Therefore, the experimental results verify that the nonlinear SAM proposed in this article has high computation accuracy.

Fig. 25 shows the cogging torque test platform. The stator is clamped by a dividing dial, and the force acts on the electronic scale at any rotor position. Then, the experimental cogging torque can be obtained by the lever principle. Fig. 26 shows the

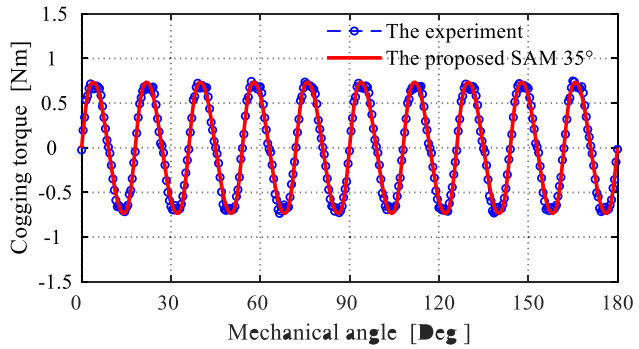

Fig. 26. Comparison of cogging torque (bonded, magnetization direction 35°).

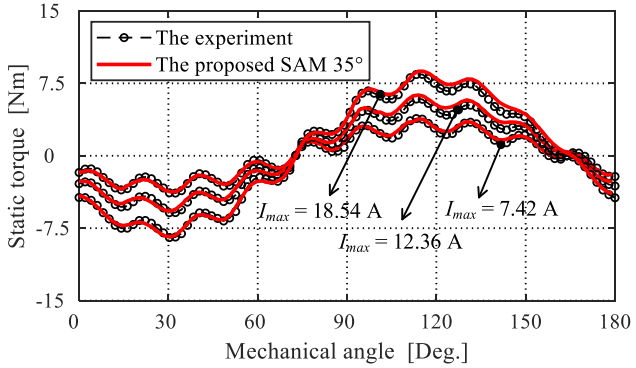

Fig. 27. Comparison of static torque (bonded, magnetization direction 35°).

comparison of cogging torque. It can be found that although the experimental cogging torque waveform at the peak is slightly different from that obtained from the SAM, it is already within the acceptable range.

Fig. 27 shows the comparison between the experimental and analytical results of static torque under different currents. In an electric period, it can be seen that the fluctuation trend of the static torque waveform obtained by the experiment and the nonlinear SAM is consistent. When the maximum current is 12.36 A (i.e., $i_a = 12.36$ A, $i_b = i_e = 3.82$ A, and $i_c = i_d = -10$ A), the maximum static torque obtained by the experiment and the nonlinear SAM is 5.89 and 6.15 N · m, respectively, and the relative error is 4.41%, which meets the error requirements.

VI. Conclusion

In this article, a nonlinear SAM is presented for magnetic field prediction for a multiphase Halbach array AFPMM. The permeability of ferromagnetic materials is considered in the analytical model. In particular, to consider local magnetic saturation, the iron parts are divided into smaller parts along both θ- and z-directions, and the permeability of each part is obtained by an iterative algorithm. The proposed method has a great engineering application value for the design and optimization of AFPMM with a multiphase Halbach array structure. Moreover, the developed SAM can be applied to other types of machines equipped with Halbach array PMs, for instance, the multiphase linear PM machines, and other electromagnetic analysis models based on the Cartesian coordinates. A fast and efficient multiobjective optimization strategy of multiphase Halbach array AFPMM combined with nonlinear SAM and NSGA-II algorithm will be studied in the future.

References

[1] J. F. Gieras, R.-J. Wang, and M. J. Kamper, *Axial Flux Permanent Magnet Brushless Machines*. New York, NY, USA: Springer, 2008.

[2] M. Lampérth, A. Malloy, A. Mlot, and M. Cordner, "Assessment of axial flux motor technology for hybrid powertrain integration," *World Electr. Vehicle J.*, vol. 7, no. 2, pp. 187–194, Jun. 2015, doi: 10.3390/wevj7020187.

[3] Z. Zhang, C. Wang, and W. Geng, "Design and optimization of Halbach-array PM rotor for high-speed axial-flux permanent magnet machine with ironless stator," *IEEE Trans. Ind. Electron.*, vol. 67, no. 9, pp. 7269–7279, Sep. 2020, doi: 10.1109/TIE.2019.2944033.

[4] X.-Y. Wang, X. Li, C.-P. Li, S.-J. Xu, and L.-T. Ling, "Design of a PCB stator coreless axial flux permanent magnet synchronous motor based on a novel topology Halbach array," *Frontiers Inf. Technol. Electron. Eng.*, vol. 20, no. 3, pp. 414–424, Mar. 2019, doi: 10.1631/FITEE.1700345.

[5] S. Neethu, S. P. Nikam, S. Singh, S. Pal, A. K. Wankhede, and B. G. Fernandes, "High-speed coreless axial-flux permanent-magnet motor with printed circuit board winding," *IEEE Trans. Ind. Appl.*, vol. 55, no. 2, pp. 1954–1962, Mar. 2019, doi: 10.1109/TIA.2018.2872155.

[6] W. Geng and Z. Zhang, "Analysis and implementation of new ironless stator axial-flux permanent magnet machine with concentrated nonoverlapping windings," *IEEE Trans. Energy Convers.*, vol. 33, no. 3, pp. 1274–1284, Sep. 2018, doi: 10.1109/TEC.2018.2799172.

[7] P. Jin, Y. Yuan, Q. Xu, S. Fang, H. Lin, and S. L. Ho, "Analysis of axial-flux Halbach permanent-magnet machine," *IEEE Trans. Magn.*, vol. 51, no. 11, pp. 1–4, Nov. 2015, doi: 10.1109/TMAG.2015.2449352.

[8] B. Guo, Y. Huang, F. Peng, J. Dong, and Y. Li, "Analytical modeling of misalignment in axial flux permanent magnet machine," *IEEE Trans. Ind. Electron.*, vol. 67, no. 6, pp. 4433–4443, Jun. 2020, doi: 10.1109/TIE.2019.2924607.

[9] H. Tiegna, A. Bellara, Y. Amara, and G. Barakat, "Analytical modeling of the open-circuit magnetic field in axial flux permanent-magnet machines with semi-closed slots," *IEEE Trans. Magn.*, vol. 48, no. 3, pp. 1212–1226, Mar. 2012, doi: 10.1109/TMAG.2011.2171979.

[10] X. Dai, Q. Liang, J. Cao, Y. Long, J. Mo, and S. Wang, "Analytical modeling of axial-flux permanent magnet eddy current couplings with a slotted conductor topology," *IEEE Trans. Magn.*, vol. 52, no. 2, pp. 1–15, Feb. 2016, doi: 10.1109/TMAG.2015.2493139.

[11] J. Y. Choi, S. H. Lee, K. J. Ko, and S. M. Jang, "Improved analytical model for electromagnetic analysis of axial flux machines with double-sided permanent magnet rotor and coreless stator windings," *IEEE Trans. Magn.*, vol. 47, no. 10, pp. 2760–2763, Oct. 2011, doi: 10.1109/TMAG.2011.2151840.

[12] A. Bellara, Y. Amara, G. Barakat, and P. Reghem, "Analytical modelling of the magnetic field in axial flux permanent magnet machines with semi-closed slots at no load," in *Proc. XIX Int. Conf. Electr. Mach. (ICEM)*, Sep. 2010, pp. 1–6, doi: 10.1109/ICELMACH.2010.5607988.

[13] B. Guo, Y. Huang, F. Peng, and J. Dong, "General analytical modeling for magnet demagnetization in surface mounted permanent magnet machines," *IEEE Trans. Ind. Electron.*, vol. 66, no. 8, pp. 5830–5838, Aug. 2019, doi: 10.1109/TIE.2018.2873099.

[14] A. Mohammadi, H. Mirzamani, A. Oraee, and S. Taghipour Boroujeni, "Approach for analytical modelling of axial-flux PM machines," *IET Electr. Power Appl.*, vol. 10, no. 6, pp. 441–450, Apr. 2016, doi: 10.1049/iet-epa.2015.0645.

[15] Q. Li, B. Zhang, and A. Liu, "Electromagnetic force analysis of eccentric axial flux permanent magnet machines," *Math. Problems Eng.*, vol. 2020, Apr. 2020, Art. no. e6194317, doi: 10.1155/2020/6194317.

[16] A. Daghigh, H. Javadi, and A. Javadi, "Improved analytical modeling of permanent magnet leakage flux in design of the coreless axial flux permanent magnet Generatorx," *Can. J. Elect. Comput. Eng.*, vol. 40, no. 1, pp. 3–11, 2017, doi: 10.1109/CJECE.2016.2550667.

[17] Y. Kano, T. Kosaka, and N. Matsui, "A simple nonlinear magnetic analysis for axial-flux permanent-magnet machines," *IEEE Trans. Ind. Electron.*, vol. 57, no. 6, pp. 2124–2133, Jun. 2010, doi: 10.1109/TIE.2009.2034685.

[18] A. Hemeida et al., "A simple and efficient quasi-3D magnetic equivalent circuit for surface axial flux permanent magnet synchronous machines," *IEEE Trans. Ind. Electron.*, vol. 66, no. 11, pp. 8318–8333, Nov. 2019, doi: 10.1109/TIE.2018.2884212.

[19] R. Alipour-Sarabi, Z. Nasiri-Gheidari, and H. Oraee, "Development of a three-dimensional magnetic equivalent circuit model for axial flux machines," *IEEE Trans. Ind. Electron.*, vol. 67, no. 7, pp. 5758–5767, Jul. 2020, doi: 10.1109/TIE.2019.2934065.
[20] H. Zhao, K. T. Chau, T. Yang, Z. Song, and C. Liu, "A novel quasi-3D analytical model for axial flux motors considering magnetic saturation," *IEEE Trans. Energy Convers.*, vol. 37, no. 2, pp. 1358–1368, Jun. 2022, doi: 10.1109/TEC.2021.3132618.
[21] R. L. J. Sprangers, J. J. H. Paulides, B. L. J. Gysen, and E. A. Lomonova, "Magnetic saturation in semi-analytical harmonic modeling for electric machine analysis," *IEEE Trans. Magn.*, vol. 52, no. 2, pp. 1–10, Feb. 2016, doi: 10.1109/TMAG.2015.2480708.
[22] Z. Djelloul-Khedda, K. Boughrara, F. Dubas, and R. Ibtiouen, "Nonlinear analytical prediction of magnetic field and electromagnetic performances in switched reluctance machines," *IEEE Trans. Magn.*, vol. 53, no. 7, pp. 1–11, Jul. 2017, doi: 10.1109/TMAG.2017.2679686.
[23] Z. Djelloul-Khedda, K. Boughrara, R. Ibtiouen, and F. Dubas, "Nonlinear analytical calculation of magnetic field and torque of switched reluctance machines," in *Proc. Int. Conf. Electr. Sci. Technol. Maghreb (CISTEM)*, Oct. 2016, pp. 1–8, doi: 10.1109/CISTEM.2016.8066773.
[24] Z. Djelloul-Khedda, K. Boughrara, F. Dubas, A. Kechroud, and A. Tikellaline, "Analytical prediction of iron-core losses in flux-modulated permanent-magnet synchronous machines," *IEEE Trans. Magn.*, vol. 55, no. 1, pp. 1–12, Jan. 2019, doi: 10.1109/TMAG.2018.2877164.
[25] H. Zhao, C. Liu, Z. Song, and W. Wang, "Exact modeling and multiobjective optimization of Vernier machines," *IEEE Trans. Ind. Electron.*, vol. 68, no. 12, pp. 11740–11751, Dec. 2021, doi: 10.1109/TIE.2020.3044785.
[26] H. Zhao, C. Liu, Z. Song, and J. Yu, "A fast optimization scheme of coaxial magnetic gears based on exact analytical model considering magnetic saturation," *IEEE Trans. Ind. Appl.*, vol. 57, no. 1, pp. 437–447, Jan. 2021, doi: 10.1109/TIA.2020.3040142.
[27] B. Guo et al., "Nonlinear semianalytical model for axial flux permanent-magnet machine," *IEEE Trans. Ind. Electron.*, vol. 69, no. 10, pp. 9804–9816, Oct. 2022, doi: 10.1109/TIE.2022.3159952.
[28] Z. Song, C. Liu, K. Feng, H. Zhao, and J. Yu, "Field prediction and validation of a slotless segmented-Halbach permanent magnet synchronous machine for more electric aircraft," *IEEE Trans. Transport. Electrific.*, vol. 6, no. 4, pp. 1577–1591, Dec. 2020, doi: 10.1109/TTE.2020.2982733.
[29] H. S. Zhang, Z. X. Deng, M. L. Yang, Y. Zhang, J. Y. Tuo, and J. Xu, "Analytical prediction of Halbach array permanent magnet machines considering finite tooth permeability," *IEEE Trans. Magn.*, vol. 56, no. 6, pp. 1–10, Jun. 2020, doi: 10.1109/TMAG.2020.2982844.
[30] Y. Shen and Z. Q. Zhu, "Investigation of permanent magnet brushless machines having unequal-magnet height pole," *IEEE Trans. Magn.*, vol. 48, no. 12, pp. 4815–4830, Dec. 2012, doi: 10.1109/TMAG.2012.2202398.
[31] Z. Djelloul-Khedda, K. Boughrara, F. Dubas, A. Kechroud, and B. Souleyman, "Semi-analytical magnetic field predicting in many structures of permanent-magnet synchronous machines considering the iron permeability," *IEEE Trans. Magn.*, vol. 54, no. 7, pp. 1–21, Jul. 2018, doi: 10.1109/TMAG.2018.2824278.
[32] A. Hemeida and P. Sergeant, "Analytical modeling of surface PMSM using a combined solution of Maxwell–s equations and magnetic equivalent circuit," *IEEE Trans. Magn.*, vol. 50, no. 12, Dec. 2014, Art. no. 7027913, doi: 10.1109/TMAG.2014.2330801.

Yunlu Du (Graduate Student Member, IEEE) received the B.S. degree in electrical engineering from Anhui University, Hefei, China, in 2020. He is currently pursuing the Ph.D. degree with the School of Electrical Engineering, Southeast University, Nanjing, China.

His main research interests include electromagnetic field computation and permanent magnet (PM) motor design.

Yunkai Huang received the M.Sc. and Ph.D. degrees in electrical engineering from Southeast University, Nanjing, China, in 2001 and 2007, respectively.

He is currently a Professor with the School of Electrical Engineering, Southeast University, where he has been teaching electrical machinery and digital signal processing. His research interests include the design and control of permanent magnet (PM) machine and high-speed machine, applications in domestic appliances, electric vehicles, railway traction, all-electric ships, and wind power generation systems.

Baocheng Guo (Member, IEEE) received the B.E. degree in electrical engineering from the China University of Petroleum, Qingdao, China, in 2009, the M.E. degree in electrical engineering from the Harbin University of Science and Technology, Harbin, China, in 2014, and the Ph.D. degree in electrical engineering from Southeast University, Nanjing, China, in 2017.

He is currently an Assistant Professor with Nanjing Normal University (NNU), Nanjing. Before joining NNU, he was a Post-Doctoral Researcher with Southeast University. His main research interests are electromagnetic field computation and the development of fast multiphysics models of electrical machines.

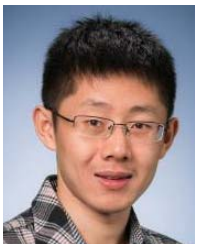

Fei Peng (Member, IEEE) received the B.S. and M.S. degrees in electrical engineering from Southeast University, Nanjing, China, in 2010 and 2012, respectively, and the Ph.D. degree in electrical and computer engineering from McMaster University, Hamilton, ON, Canada, in 2016.

After that, he was a Post-Doctoral Fellow with the McMaster Institute for Automotive Research and Technology, McMaster University. In December 2016, he joined the School of Electrical Engineering, Southeast University, as an Assistant Professor. His research interests include the optimal design and control of power converters, modeling, and the digital control of motor drives.

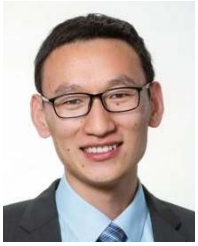

Jianning Dong (Senior Member, IEEE) received the B.S. and Ph.D. degrees in electrical engineering from Southeast University, Nanjing, China, in 2010 and 2015, respectively.

Since 2016, he has been an Assistant Professor with the DC Systems, Energy Conversion and Storage (DCE&S) Group, Delft University of Technology (TU Delft), Delft, The Netherlands. Before joining TU Delft, he was a Post-Doctoral Researcher with the McMaster Automotive Resource Centre, McMaster University, Hamilton, ON, Canada. His research interests include electromechanical energy conversion and contactless power transfer.